Nuclear Instruments and Methods in Physics Research A 786 (2015) 120–126

Contents lists available at ScienceDirect

Nuclear Instruments and Methods in Physics Research A

journal homepage: www.elsevier.com/locate/nima

Online monitoring for proton therapy: A real-time procedure using a planar PET system

A.C. Kraan [a], G. Battistoni [b], N. Belcari [a], N. Camarlinghi [a], M. Ciocca [c], A. Ferrari [d], S. Ferretti [a], A. Mairani [c], S. Molinelli [c], M. Pullia [c], P. Sala [b], G. Sportelli [a], A. Del Guerra [a], V. Rosso [a,*]

[a] Department of Physics, University of Pisa and INFN, Pisa, Italy
[b] INFN Sezione di Milano, Milano, Italy
[c] Fondazione CNAO, Pavia, Italy
[d] CERN, Geneva, Switzerland

ARTICLE INFO

Article history:
Received 21 February 2015
Received in revised form
12 March 2015
Accepted 19 March 2015
Available online 26 March 2015

Keywords:
Proton therapy
In-beam-monitoring
PET

ABSTRACT

In this study a procedure for range verification in proton therapy by means of a planar in-beam PET system is presented. The procedure consists of two steps: the measurement of the β^+-activity induced in the irradiated body by the proton beam and the comparison of these distributions with simulations. The experimental data taking was performed at the CNAO center in Pavia, Italy, irradiating plastic phantoms. For two different cases we demonstrate how a real-time feedback of the delivered treatment plan can be obtained with in-beam PET imaging.

1. Introduction

In the last decades the clinical usage of particle beams as a radiotherapy modality for the treatment of solid tumors has risen considerably [1,2]. Particle beams can deliver conformal dose distributions minimizing damage to healthy tissues thanks to their deposited energy profiles characterized by the Bragg-peak. The location of the Bragg peak can be affected by different sources of range uncertainties [3] and can be different from the planned position [4]. This is particularly relevant for hypo-fractional dose schemes, i.e., treatments where the total dose is divided into a limited number of sessions. Such treatments are currently performed in standard radiotherapy [5,6] and its usage is still under discussion for particle therapy. The importance of treatment monitoring procedures in particle therapy is generally recognized [3]. Several techniques have been proposed to monitor the treatment delivered, based on different physical processes that occur in the irradiated media, like prompt-gammas [7–9], charged particles [10], β^+-emitters [11–13] or combination of these methods [14]. Although PET-imaging has been mostly used for a-posteriori treatment monitoring, in-beam PET imaging during dose delivery is attractive, because it allows to detect shorter-lived isotopes like ^{15}O ($t_{1/2}$=2.0 min), and minimizes washout problems [4].

In this study we present a monitoring procedure of two proton treatment sessions, by measuring the β^+-activity generated in plastic phantoms by the proton beam. In particular, we will demonstrate how our in-beam PET system can provide feedback already at early stages of the treatment fraction, before full dose is delivered. The annihilation photons generated by the β^+ activity were acquired using an "ad hoc" developed planar PET system. The monitoring procedure consisted of the simulation of the expected 3D β^+-activity distribution prior to the treatment delivery, pre-calculated, and the comparison of the pre-calculated distributions with the experimental ones. To demonstrate the capabilities of the proposed monitoring procedure an experimental data taking was performed at CNAO center in Pavia, Italy, where homogeneous 2 Gy treatment plans were delivered onto plastic phantoms.

2. Methods and materials

2.1. The detection system

We used a dual head planar Positron Emission Tomography (PET) system called DoPET, developed for the monitoring of particle treatments. The two stationary opposite heads were the detecting blocks of the system and had a surface of approximately 10×10 cm^2 each. Each head was composed of 4 (2×2) independent modules. Each module consisted of an H8500 PMT coupled to a 23×23 LYSO crystal matrix (2 mm pitch) with the readout performed by custom developed electronics. The two heads could be positioned at different distances. For the data taking discussed in this paper the distance was fixed at 20 cm.

* Corresponding author.
E-mail address: valeria.rosso@pi.infn.it (V. Rosso).

http://dx.doi.org/10.1016/j.nima.2015.03.059
0168-9002/

The Data Acquisition (DAQ) was designed to keep the acquisition dead time low and to have a relatively narrow coincidence window (3 ns). Coincidences were performed in AND-gating mode: each module on one head with all the modules of the opposite head [15]. More details about the DoPET system and its experimental results are reported in [16–18].

2.2. Irradiation and phantom characteristics

A Treatment Plan (TP) delivering a uniform dose of 2 Gy to a $3 \times 3 \times 3$ cm^3 Planning Target Volume (PTV) was used for this paper. The PTV was located centrally in a $8 \times 8 \times 7$ cm^3 Poly-MethylMethAcrylate (PMMA) phantom in between 3 cm and 6 cm water equivalent depth. The irradiation was performed at the Centro Nazionale di Adroterapia Oncologica (CNAO) located in Pavia, Italy, a synchrotron based facility treating patients since September 2011 [19]. In Fig. 1, the DoPET system set up on the treatment couch together with the DAQ boards and the power supplies are shown.

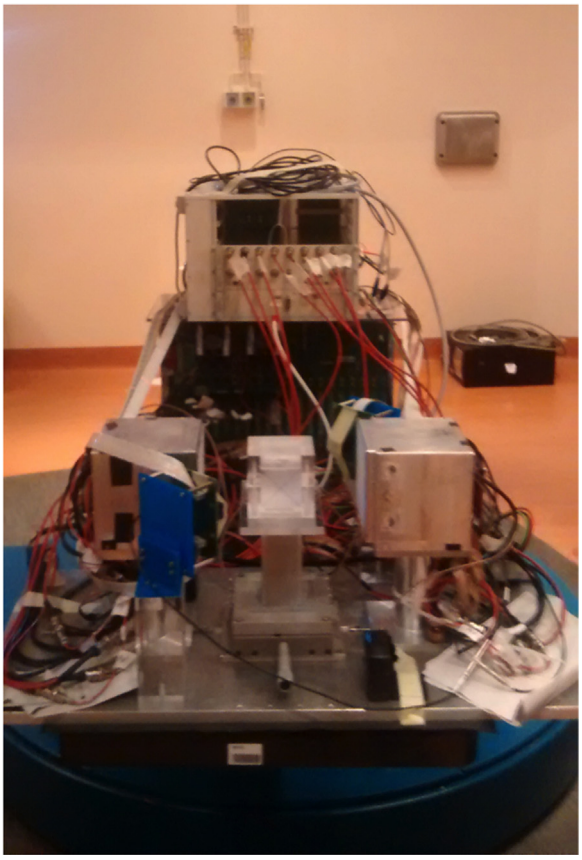

Fig. 1. The DoPET system on the treatment couch at CNAO during the installation phase. The PMMA phantom is visible in between the two PET heads.

The CNAO spill structure was characterized by 1 s of irradiation (in-spill) followed by 4 s of pause (inter-spill), and data were tagged accordingly. The TP was made using a commercial planning system (Syngo PT Planning VC12, Siemens). The selected 2 Gy cubic TP was delivered in 146 s using 17 different proton beam energies, called iso-energy layers, starting from 62.3 MeV up to 90.8 MeV. No ripple filter was used during the irradiation.

Fig. 2 shows the number of protons per energy layer and their temporal delivery. The small peak in Fig. 2 (left) is intrinsic to the TP. The sequence of energy layers was chosen in such a way that each energy increment corresponded to a proton range increase 2 mm in water, i.e., 1.7 mm in PMMA depth.

In order to deliver a homogeneous dose to the selected 27 cm^3 PTV, the number of protons per layer increased for higher energies, as reported in Fig. 2 (left). As the proton number increased, the dose delivery time for more energetic layers increased as well (Fig. 2, right). More than one third of the total plan delivery time was necessary to deliver the last two energies layers. The expected proton range, corresponding to each energy layer, is also reported in Fig. 2 (right): the proton irradiation is performed from the proximal (closer to the beam entrance surface) to the distal (farther with respect to the beam entrance surface) target slices.

Two different phantoms were irradiated: a uniform PMMA phantom, and a PMMA phantom with an air-cavity. Both phantoms had a section of 8×8 cm^2 in the transversal direction and 7 cm in the beam direction. The heterogeneous phantom was obtained from a uniform PMMA block containing a cylindrical air cavity of 34 mm diameter and 5 mm height starting at a depth of 4 cm from the beam entrance surface.

2.3. Monte Carlo simulations

The proton interactions in PMMA and the calculation of the induced β^+-activity distribution were performed using the FLUKA Monte Carlo code [20,21]. Although other MC codes are used in proton therapy, like GEANT [22,23] and MCNP [24,25], we chose to use FLUKA, because of prior usage [26] and because FLUKA has been thoroughly validated for PET studies [3,26,32]. The FLUKA simulation included the CNAO beam line simulation [26,27,28] and the phantom geometry. At this stage, neither the detector geometry nor the DAQ

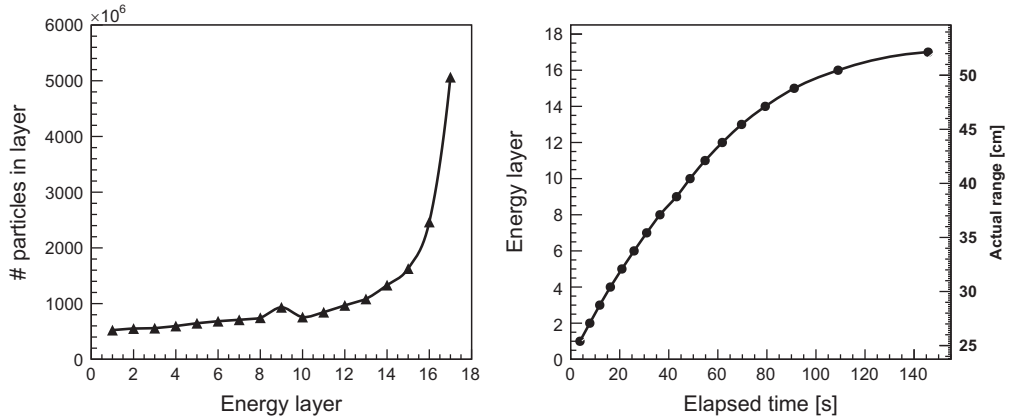

Fig. 2. The number of proton per layer (left) and the corresponding temporal delivery profile (right) for a 2 Gy homogeneous TP on PMMA phantom. Each dot reported in the figure (right) corresponds to the end time of the delivery of each energy layer. The corresponding proton range is also reported on the right vertical axis for energies from 62.3 MeV up to 90.8 MeV.

characteristics were simulated. The position of the production and decay of the β^+-emitting isotopes was scored, as well as the isotope type and decay time.

Dose and activity are arising from different physics processes, as can be seen from Fig. 3, where the activity profile (red line) and the dose profile (black), are reported for the 2 Gy TP from Section 2.2, delivered to the homogeneous PMMA phantom. The dose profile is the convolution of 17 Bragg peaks. The absence of the ripple filter during irradiation explains the rippled non-uniform dose. The entrance surface of the phantoms is located at the position $z=0$. The activity distribution profile in Fig. 3 is the integral calculated from the beginning of the irradiation up to 3 min, i.e., for an online measurement, here plotted without separate in-spill and inter-spill phases. Looking at Fig. 3, the activity profile stops several millimeters before the most distal Bragg-peak, as the protons, at the end of their path, do not have sufficient energy anymore to produce β^+-emitting fragments.

2.4. Raw-data processing, reconstruction and 1-D activity profiles

Data acquired by the DoPET system were stored in a "list mode" format containing the information of the photon impinging point and the deposited energy. A Maximum Likelihood Estimation Maximization (MLEM) LOR based algorithm was implemented to reconstruct a field of view of $10\times10\times10$ cm^3 volume segmented in 1 mm^3 voxels.

The reconstruction software used a system response matrix: the matrix was evaluated using a multi-ray algorithm [29]. Acquired data could be transformed in a 3-D measured activity distribution in less than 1 min using an 8 core Intel Xeon e5620 @2.4 GHz. To improve the detector uniformity response, a direct normalization procedure, already described in [17], was performed before the reconstruction function, using an extended planar ($11\times11\times0.3$ cm^3) phantom filled with a water solution containing ^{18}F, a β^+-emitter.

From the experimental 3-D reconstructed activity distribution 1-D activity profiles were calculated using an analysis platform based on ROOT. The z-axis was set along the beam direction.

2.5. Monitoring procedure

To verify the correctness of the beam delivery we compared the expected β^+-activity distributions, calculated with the FLUKA Monte Carlo code, with the experimental data. The experimental data were acquired performing an online measurement, summing up "in-spill" and "inter-spill" phases. However, in the post-processing phase, the data were divided into frames starting from the beginning of the acquisition and ending at 30, 60, 90, 120, 150, and 180 s, with 146 s being the TP planned delivery duration.

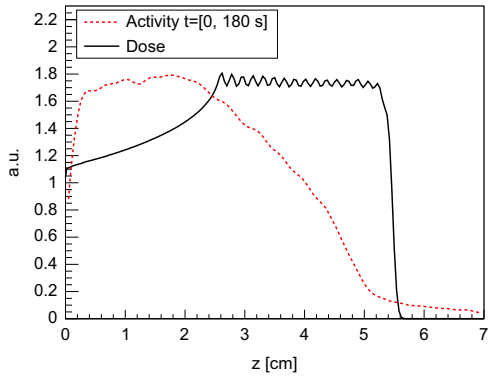

Fig. 3. Dose and activity profiles simulated by FLUKA for a 2 Gy uniform TP irradiating a PMMA phantom. The z axis represents the beam direction. The dose profile is not flat as no ripple filter was adopted during the irradiation. (For interpretation of the references to color in this figure legend, the reader is referred to the web version of this article.)

The beam direction (z) was a privileged axis due to the geometrical configuration of the PET system. As already reported previously [17,30], along this direction the DoPET system has the capability to detect position variation down to a millimeter.

1-D activity profiles, along the beam direction (z axis), were obtained projecting all the activity annihilation points inside the selected volume on the z-axis. Only volumes that were symmetric with respect to the beam direction, like a flattened cylinder with an elliptic section, were selected, as already described in [31]. The extension of the considered volume cylinder transversal surface could be varied, according to the phantom under study.

The choice to consider a discrete volume to calculate the 1-D profile instead of simply extract a line-profile from the 3-D activity distribution was done to overcome the limited number of annihilation events detected during the early acquisitions.

3. Results

3.1. Monte Carlo simulation results for the homogeneous phantom

In order to understand the contributions of the various isotopes, we first analyzed the true Monte Carlo activity distributions, resulting from the simulation of the 2 Gy TP delivered on the homogeneous PMMA phantom. Fig. 4 shows the contributions of the most abundant β^+-emitters isotopes as obtained with the FLUKA Monte Carlo simulations for different time intervals, all starting at the beginning of the irradiation, and including in-spill and inter-spill contributions.

The first 1-D activity profile of Fig. 4 was calculated when less than one fifth of the total protons of the TP were delivered in the phantom, that is, after only 30 s from the beginning of the irradiation. Looking at the profiles of Fig. 4 we see how the activated volume grows with time, following the TP delivery. As a result, the fall-off shape changes with time: the profiles are calculated from integral measurements starting from the beginning of the irradiation and therefore the contribution to the activity profile of the first volume layers of the PTV is greater with respect to the contributions of the following layers.

All the profiles of Fig. 4 are characterized by long tails, which are the result of prompt-γ events and other short-lived isotopes like ^{8}B ($t_{1/2}=770$ ms) and ^{12}N ($t_{1/2}=11$ ms), which have a relative strong contribution when considering small time intervals during irradiation.

The abundance of produced isotopes at different times was calculated and is reported in Table 1. The associated errors, due to statistical fluctuations, were evaluated for all isotopes. For time intervals greater than 30s the errors were equal or less than 0.1%, while for the first interval, $\Delta t=30$ s, the errors were equal or lower than 0.2%. The prompt-γ events contribution is summed together with the contribution of other isotopes, and reported in the column labeled "Other".

3.2. DoPET system data analysis: Results

The experimental data taking that corresponds to the experimental configuration simulated in Section 2.1, was performed at CNAO.

To easily compare the experimental with the simulated data, in Fig. 5 we report the experimental profiles (black line), and the FLUKA 1-D (light brown) activity profiles for the corresponding times. For each time interval, both the MC and experimental data are normalized to the same area. As no activity is expected before

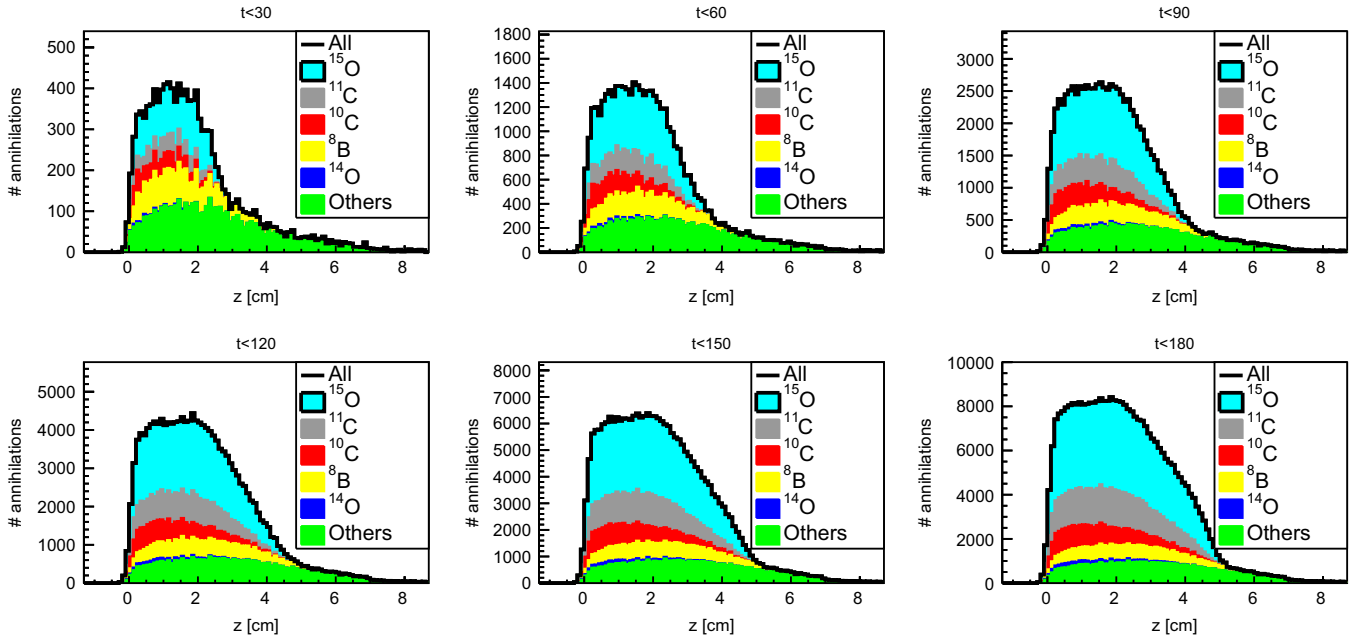

Fig. 4. Monte Carlo 1-D activity profiles along the beam direction during the delivery of the 2 Gy uniform TP, at 30, 60, 90, 120, 150 and 180 s from the beginning of the irradiation. The produced isotopes and their percentage are reported in different colors. In the histograms the abundance of each isotope is proportional to the corresponding colored area. The homogeneous PMMA phantom starts at $z=0$.

Table 1
Percentage of the produced isotopes relative to the profiles reported in Fig. 4. The profiles are relative to a uniform 2 Gy TP (see Fig. 2 for details) delivered on a PMMA phantom.

Time [s]	^{15}O (%)	^{11}C (%)	^{10}C (%)	^{8}B (%)	^{14}O (%)	Other (%)
30	27.0	8.6	7.6	18.3	0.7	37.7
60	34.4	11.8	9.6	14.7	1.0	28.5
90	38.4	13.9	9.7	12.6	1.1	24.3
120	40.4	15.0	9.7	11.7	1.2	22.0
150	44.1	17.1	9.7	9.4	1.4	18.4
180	47.1	19.3	8.8	7.6	1.4	15.7

the irradiated phantom, the data with z lower than zero were discarded for the normalization. The agreement between experimental and simulated data was satisfactory.

The shape of the 1-D activity profiles appears distorted with respect to the simulated profiles. Several effects explain the difference. First, as already reported in [31], the difference in shape of the 1-D activity profiles is due to the fact that the DoPET system has a limited angular coverage while the Monte Carlo profiles are the result of a total coverage angle simulation. Second, the effective time delivery of the energy layers of the TP is not precisely known. As discussed before, in the proposed procedure we compare pre-calculated Monte Carlo profile with the experimental profiles, and small variations in the TP delivery time or beam intensity may influence the experimental 1-D activity profiles. In Fig. 5 the mismatch is more evident at earlier times ($\Delta t=30$ and 60 s) and less visible for the last acquisitions. Third, the experimental 1-D activity profile data present a bump before $z=0$, so outside the activated volume, and a tail with somewhat different amplitude with respect to the Monte Carlo profiles. This is being investigated, and we expect that it will be less evident with bigger detectors.

Despite the differences in shape, the distal fall-off position of the measured 1-D activity profiles matched very well the Monte Carlo expectations, especially at higher acquisition times. The experimental acquisition at $t=30$ s was very challenging due to the very low statistics: in fact the first histogram of Fig. 5 has a very limited number of counts per bin, and the statistical fluctuations, evaluated as the square root of the number of counts with respect to the total counts per pixels is up to 20% for the smallest statistics bins. This uncertainty decreases for longer acquisitions where the statistical error is of the order of few %.

3.3. Monte Carlo and DoPET data comparison for a homogeneous phantom

For the different time-intervals we compared the activity profile width at 50%, $\Delta W_{50\%}$, between expected and experimental data, as was done in previous works [32–34]. Here $\Delta W_{50\%}$ was defined as the distance along the beam direction between the position of the activity proximal rise at 50% of the associated local maximum, and the position of the activity distal fall-off at 50% of the associated local maximum. As a visual guide for the calculation of the $\Delta W_{50\%}$ in all histograms of Fig. 5 the 50% activity rise position and the local maximum points are reported in red; likewise the 50% activity fall-off position and maximum are reported in blue (in top left and top right plot the red and blue vertical lines of the local maximum positions overlap).

The $\Delta W_{50\%}$ at different times (30, 60, 90, 120, 150 and 180 s after the beginning of the irradiation) was calculated from the histograms reported in Figs. 4 and 5 and is shown in Fig. 6. The error bars reported in Fig. 6 represent only the statistical fluctuations of the activity profiles bin data, evaluated as reported in [35]. The errors are roughly 0.1% and are visible only for earlier acquisitions where the statistics are low and the effect of fluctuations are more relevant.

Fig. 6 shows that the agreement between the experimental data, black circles, and the Monte Carlo predictions, red squares, is good. Even at small times, the DoPET system could detect variations of the $\Delta W_{50\%}$ value. The system characteristics are such that a real-time response on the activity width during data-acquisition is possible, even before full dose was delivered.

3.4. Monte Carlo and DoPET data comparison for a heterogeneous phantom

In order to understand the feedback of the system for a non-homogeneous phantom, a PMMA phantom with an air-cavity was

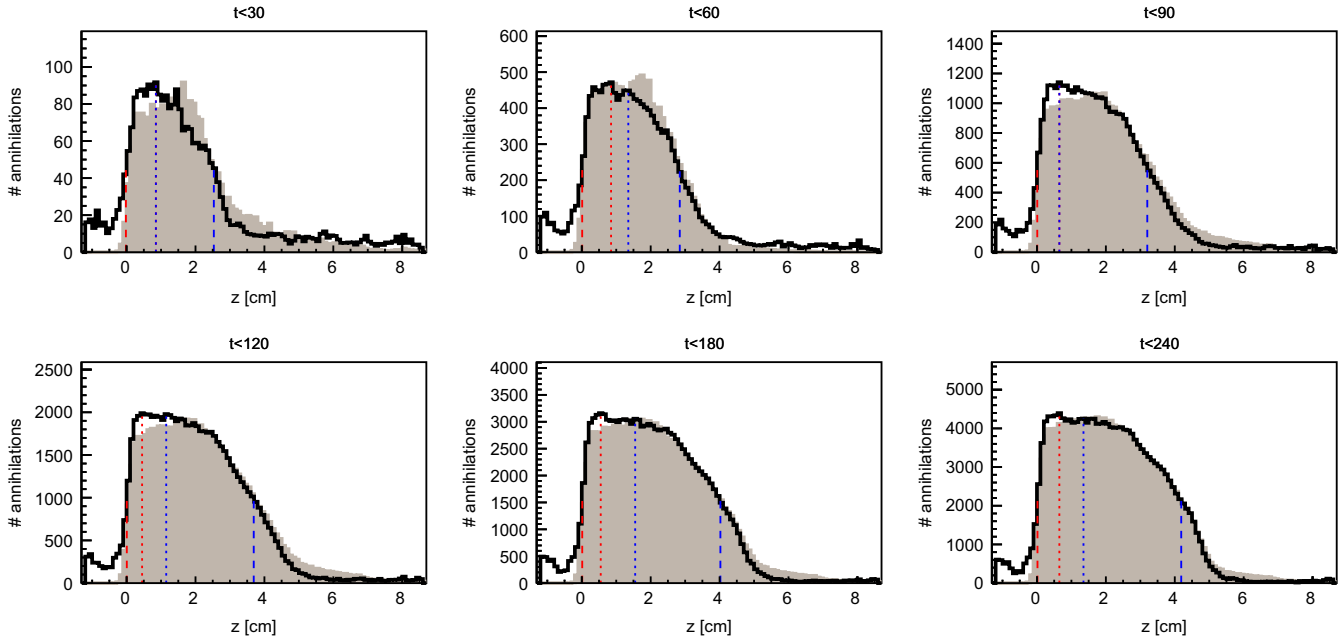

Fig. 5. Experimental 1-D activity profiles, for a homogeneous PMMA phantom, along the beam direction at 30, 60, 90, 120, 150 and 180 s from the beginning of the irradiation. The experimental data, black line, are superimposed to the corresponding Monte Carlo simulation profile, light brown area. The profiles are normalized. The vertical segmented lines represent in red the 50% positions for the activity rise and the local maximum of the considered interval; likewise the blue segmented lines report the local maximum of the fall-off used interval and the 50% fall-off positions (see also text). (For interpretation of the references to color in this figure legend, the reader is referred to the web version of this article.)

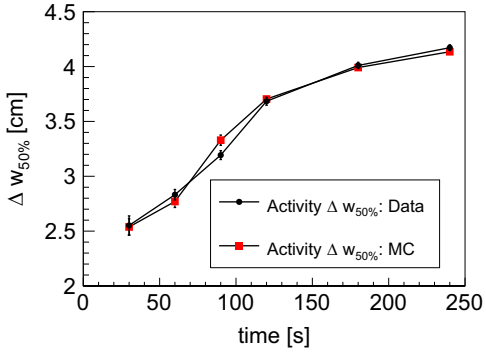

Fig. 6. Comparison between the experimental $\Delta W_{50\%}$ values (black circles) and the calculated ones (red squares) at 30, 60, 90, 120, 150 and 180 s from the beginning of the irradiation. The error bars represent the incidence of statistical fluctuations. (For interpretation of the references to color in this figure legend, the reader is referred to the web version of this article.)

irradiated at CNAO with the same TP as described in 2.2. In Fig. 7 the 1-D activity profile histograms at different times for the Monte Carlo simulations, in light brown, and for the obtained experimental 1-D activity profiles, black line, are reported; the Monte Carlo profiles were normalized so that the two profiles have the same area, hereby again discarding the data for z lower than zero as done in Fig. 5.

The presence of the air cavity in the phantom caused a beam overshoot, represented by an extended profile tail, visible in both the Monte Carlo simulation and in the experimental 1-D activity profiles. In the Monte Carlo profiles the local decrease is more pronounced than in data, mostly due to the limited solid angle coverage of the experimental system and associated experimental resolution, as was mentioned in Section 3.2.

It must be noted that the air-cavity was located deep inside the phantom (at 4 cm), and the beam reached it only after 40 s from the beginning of the TP delivery, as can be seen from Fig. 2 (right). As a consequence, the air-cavity presence becomes visible only in the last 3 plots of Fig. 7. It must be noted that the selected volume for the profiles in Fig. 7 is smaller than that in Fig. 5 in order to better highlight the presence of the air-cavity, and as a consequence the number of detected annihilations is smaller than that reported in Fig. 5.

In terms of detectability, the position of the air-cavity, being located along the fall-off zone, was challenging for the system, but still successful.

In this case the activity width ($\Delta W_{50\%}$), was not a good parameter as the air-cavity is located after the 50% of the distal fall-off, as shown in Fig. 7.

4. Discussion

In this study we described a procedure for the monitoring of proton therapy that is based on a comparison of the measured and pre-calculated β^+-activity profiles. In particular, we performed the comparison at 30, 60, 90, 120, 150 and 180 s from the beginning of the delivery of a 2 Gy uniform TP to demonstrate that the monitoring is possible also at early phases. The $\Delta t = 30$ s is the earliest time at which the DoPET system was able to measure the 1-D activity profile (see Figs. 5 and 7), even if the number of protons was limited and represented only a small fraction of the total TP proton number (see Fig. 2 left).

The presented procedure allows monitoring the TP delivery following the activation of the irradiated volume and permits to localize changes, if any, along the protons path (see Fig. 7). These results indicate that the PET technique can be used to check the treatment in hypo-fractional dose scheme using only a fraction of the planned dose. For this application it could be advisable to start the treatment with protons belonging to the most energetic energy layers, not only because in this way the entire volume covered by the treatment can be monitored, but also because the higher energetic spots contain more protons.

By comparing the experimental data with the Monte Carlo simulations we have the evidence that the DoPET system is partially paralyzed during the spill delivery and loses a fraction of the in-spill

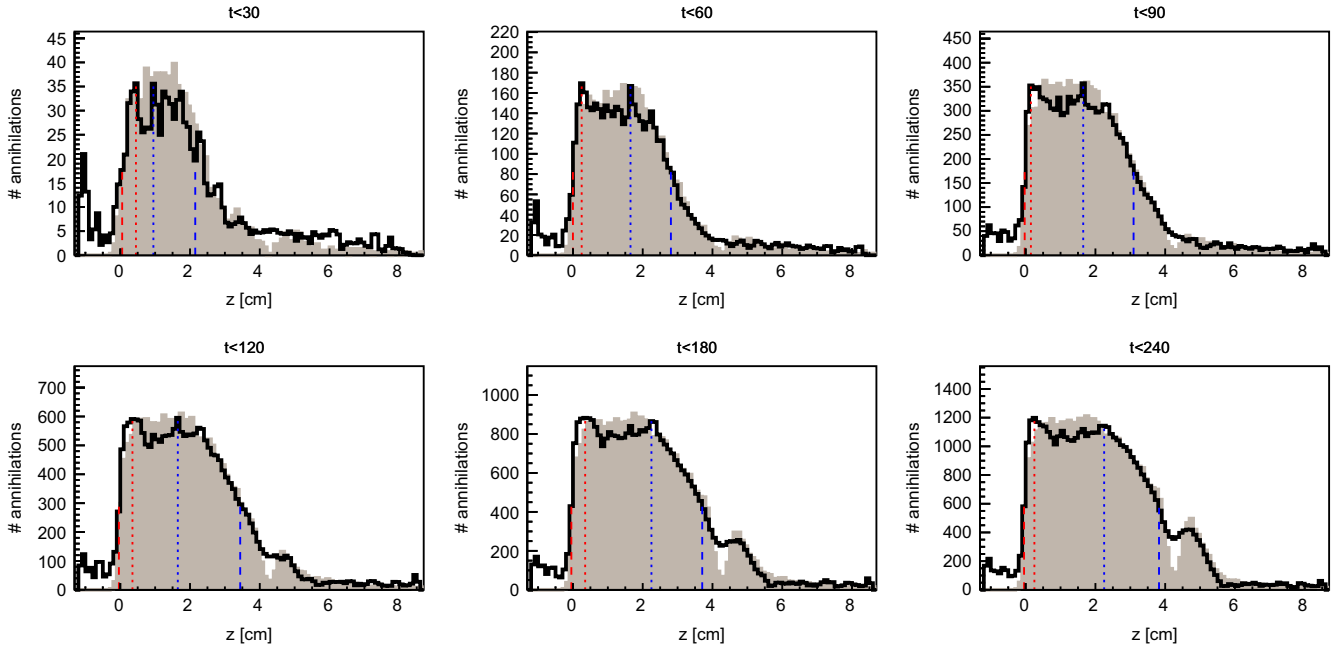

Fig. 7. Experimental 1-D activity distributions along the beam direction at 30, 60, 90, 120, 150 and 180 s from the beginning of the irradiation for the PMMA phantom with an air cavity. The air-cavity creates a plateau in the experimental data. The experimental data, black line, are superimposed to the corresponding Monte Carlo data, light brown area. The profiles are normalized.

events. We verified, both experimentally and by Monte Carlo simulations, that this problem is more evident when the used accelerator is a synchrotron as opposed to a cyclotron [18,31].

5. Conclusions

Comparing the 1-D activity profiles measured by the DoPET system with the one pre-calculated using the FLUKA MC code, we applied a real-time TP monitoring procedure in proton therapy. We demonstrated that the DoPET system was able to provide a reliable feedback also at very early phases of the treatment, much before the full dose was delivered.

The proposed real-time monitoring modality does not increase the occupancy of the treatment room, is less affected by washout phenomena and detects also small anomalies, like a small air cavity, giving a real-time feedback.

A new prototype with an extended area of 15×15 cm^2 is currently under construction, which will be able to monitor anatomic phantoms with larger irradiated volumes. It will be tested in the near future.

Acknowledgements

This research has been supported by the FULLBEAM-300838 Marie Curie Intra European Fellowship within the 7th European Community Framework Program, and by the INFN-RT 60141 POR CRO FSE 2007-2013 fellowship.

References

[1] T.F. DeLaney, Frontiers of Radiation Therapy and Oncology 43 (2011) 465, doi:000322511.
[2] U. Amaldi, R. Bonomi, S. Braccini, M. Crescenti, A. Degiovanni, M. Garlasche', A. Garonna, G. Magrin, C. Mellace, P. Pearce, G. Pitta', P. Puggioni, E. Rosso, S. Verdu' Andres, R. Wegner, M Weiss, R. Zennaro, Nuclear Instruments and Methods A 620 (2010) 563.
[3] A.C. Knopf, A. Lomax, Physics in Medicine and Biology 58 (15) (2013) R131.
[4] W. Enghardt, K. Parodi, P. Crespo, F. Fiedler, J. Pawelke, F. Pönisch, Radiotherapy and Oncology 73 (Suppl. 2) (2004) S96.
[5] M.R. Folkert, M.H. Bilsky, A.K. Tom, J.H. Oh, K.M. Alektiar, I Laufer, W.D. Tap, Y. Yamada, International Journal of Radiation Oncology Biology Physics 88 (5) (2014) 1085.
[6] M.J. Zelefsky, C. Greco, R. Motzer, J.M. Magsanoc, X. Pei, M. Lovelock, J. Mechalakos, J. Zatcky, Z. Fuks, Y. Yamada, International Journal of Radiation Oncology Biology Physics 82 (5) (2012) 1744.
[7] J. Smeets, F. Roellinghoff, D Prieels, F. Stichelbaut, A. Benilov, P. Busca, C. Fiorini, R. Peloso, M. Basilavecchia, T Frizzi, J.C. Dehaes, A. Dubus Jun 7, Physics in Medicine and Biology 57 (11) (2012) 3371. http://dx.doi.org/10.1088/0031-9155/57/11/3371.
[8] F. Roellinghoff, M.-H. Richard, M. Chevallier, J. Constanzo, D. Dauvergne, N. Freud, P. Henriquet, F. Le Foulher, J.M. Le tang, G. Montarou, C. Ray, E. Testa, M. Testa, A.H. Walenta, Nuclear Instruments and Methods A 648 (2011) S20.
[9] JM Verburg JM, M Testa, J Seco, Physics in Medicine and Biology 60 (3) (2015) 1019. http://dx.doi.org/10.1088/0031-9155/60/3/1019.
[10] C. Agodi, G. Battistoni, F. Bellini, G.A.P. Cirrone, F. Collamati, G. Cuttone, E. De Lucia, M. De Napoli, A. Di Domenico, R. Faccini, F. Ferroni, S. Fiore, P. Gauzzi, E. Iarocci, M. Marafini, I. Mattei, S. Muraro, A. Paoloni, V. Patera, L. Piersanti, F. Romano, A. Sarti, A. Sciubba, E Vitale, C. Voenaet, Physics in Medicine and Biology 57 (2012) 5667.
[11] K. Parodi, W. Enghardt, T. Haberer, Physics in Medicine and Biology 47 (2002) 21. http://dx.doi.org/10.1088/0031-9155/47/1/302.
[12] K. Grogg, X. Zhu, C.H. Min, B. Winey, T. Bortfeld, H. Paganetti, H.A. Shih, G. El Fakhri, IEEE Transactions on Nuclear Science 60 (5) (2013) 3290.
[13] Hideaki Tashima, Taiga Yamaya, Eiji Yoshida, Shoko Kinouchi, Mitsuo Watanabe, Eiichi Tanaka, Physics in Medicine and Biology 57 (2012) 4705. http://dx.doi.org/10.1088/0031-9155/57/14/470.
[14] M. Marafini, A. Attili, G. Battistonid N. Belcari, M. G. Bisogni, N. Camarlinghi, F. Cappucci, M. Cecchetti, P. Cerello , F. Ciciriello, G.A. P. Cirrone, S. Colif, F. Corsi, G. Cuttone, E. De Lucia, S. Ferretti, R. Faccini, E. Fiorina, P. M. Frallicciardi, G. Giraudo, E. Kostarag A. Kraan, F. Licciulli, B. Liu, N. Marino, C. Marzocca, G. Matarrese, C. Morone, M. Morrocchi, S. Muraro, V. Patera, F. Pennazio, C. Peroni, L. Piersanti, M. A. Piliero, G. Pirrone, A. Rivetti, F. Romano, V. Rosso, P. Sala,A. Sarti, A. Sciubba, G. Sportelli, C. Voena, R. Wheadon, A. Del Guerra, The INSIDE project: innovative solutions for in-beam dosimetry in hadrontherapy submitted to ACTA physics polonica, in: Proceedings of II Symposium on Positron Emission Tomography, Jagiellonian University of Krakov, 21–24 September 2014.
[15] G. Sportelli, N. Belcari, P. Guerra, A. Santos, Nuclear Instruments and Methods A 648 (S1) (2011).
[16] G. Sportelli, N. Belcari, P. Guerra, F. Spinella, G. Franchi, F. Attanasi, S. Moehrs, V. Rosso, A. Santos, A. Del Guerra, IEEE Transactions on Nuclear Science 58 (3) (2011) 695.
[17] N. Camarlinghi, G. Sportelli, G Battistoni, N. Belcari, M. Cecchetti, G.A.P. Cirrone, G. Cuttone, S. Ferretti, A Kraan, A. Retico, F. Romano, P. Sala, K. Straub, A. Tramontana, A. Del Guerra, V. Rosso.#, Journal of Instrumentation 9 (04) (2014) C04005.

[18] G. Sportelli, N. Belcari, N. Camarlinghi, G.A.P. Cirrone, G. Cuttone, S. Ferretti, A. Kraan, J.E. Ortuño., F. Romano, A. Santos, K. Straub, A. Tramontana, A. Del Guerra, V. Rosso, Physics in Medicine and Biology 59 (1) (2014) 43.
[19] S. Rossi, The European Physical Journal Plus 126 (8) (2011) 78.
[20] A. Ferrari, P. Sala, A Fassò, J. Ranft, FLUKA: A Multi-Particle Transport Code (Program Version 2005), CERN, Geneva, 2005.
[21] G. Battistoni, F. Cerutti, A. Fassò, A. Ferrari, S. Muraro, J. Ranft, S. Roesler, P. Sala, AIP Conference Proceedings 896 (1) (2007) 31.
[22] S. Agostinelli, J. Allison, K . Amako, J Apostolakis, H Araujo, P. Arce, et al., Nuclear Instruments and Methods A 506 (6) (2003) 250. http://dx.doi.org/10.1016/S0168-9002(03)01368-8.
[23] G.A.P. Cirrone, G. Cuttone, S.E. Mazzaglia, F. Romano, D. Sardina, C.a Agodi, A. Attili, A. Blancato, M. De Napoli, F. Di Rosa, P. Kaitaniemi, F. Marchetto, I. Petrovic, A. Ristic-Fira, J. Shin, N. Tarnavsky, S. Tropea, C. Zacharatou, Progress in Nuclear Science and Technology 2 (2011) 207.
[24] T. Goorley, M. James, T. Booth, F. Brown, J. Bull, L.J. Cox, et al., Nuclear Technology 180 (3) (2012) 298.
[25] LANL MCNPX 2.60 Users's Guide. See: ⟨https://mcnpx.lanl.gov⟩, 2008.
[26] V. Rosso, G Battistoni, N. Belcari, N. Camarlinghi, A. Ferrari, S. Ferretti, A. Kraan, A. Mairani, N. Marino, J.E. Ortuno, M. Pullia, P. Sala, A. Santos, G. Sportelli, K. Straub, A. Del Guerra, Journal of Instrumentation 8 (C03021) (2013) 1. http://dx.doi.org/10.1088/1748-0221/8/03/C03021.
[27] T.T. Böhlen, F. Cerutti, M.P.W. Chin, A. Fassò, A. Ferrari, P.G. Ortega, A. Mairani, P. Sala, G. Smirnov, V. Vlachoudis, Nuclear Data Sheets 120 (2014) 211.
[28] T. Tessonnier, A. Mairani, F. Cappucci, A. Mirandola, G. Vilches Freixas, S. Molinelli, M. Donetti, M. Ciocca Part B, Applied Radiation and Isotopes 83 (0) (2014) 155.
[29] S. Moehrs, M. Defrise, N. Belcari, A. Del Guerra, A. Bartoli, S. Fabbri, G. Zanetti, Physics in Medicine and Biology 53 (23) (2008) 6925.
[30] S. Vecchio, F. Attanasi, N. Belcari, M. Camarda, G.A.P. Cirrone, G. Cuttone, A. Del Guerra, F. Di Rosa, N. Lanconelli, S. Moehrs, V. Rosso, G. Russo, IEEE Transactions on Nuclear Science 56 (1) (2009) 51. http://dx.doi.org/10.1109/TNS.2008.2008306.
[31] A.C. Kraan, G. Battistoni, N. Belcari, N. Camarlinghi, G.A.P. Cirrone, G. Cuttone, S. Ferretti, A. Ferrari, G. Pirrone, F. Romano, P. Sala, G. Sportelli, K. Straub, A. Tramontana, A. Del Guerra, V. Rosso, Physica Medica 30 (5) (2014) 559.
[32] K. Parodi, H. Paganetti, H.A. Shih, S. Michaud, J.S. Loeffler, T.F. DeLaney, N.J. Liebsch, J.E. Munzenrider, A.J. Fischman, A. Knopf, T. Bortfeld, International Journal of Radiation Oncology Biology Physics 68 (2007) 920.
[33] G. Sportelli, K. Straub, M. Aiello, F. Attanasi, N. Belcari, N. Camarlinghi, G.A.P. Cirrone, G. Cuttone, S. Ferretti, N. Marino, D. Nicolosi, F. Romano, V. Rosso, Nuclear Instruments and Methods A 718 (2013) 151.
[34] X. Zhu, G. El Fakhri, Theranostics 3 (10) (2013) 731.
[35] A.C. Kraan, G. Battistoni, N. Belcari, N. Camarlinghi, F. Cappucci, M Ciocca, A. Ferrari, S. Ferretti, A. Mairani, S. Molinelli, M. Pullia, A. Retico, P. Sala, G. Sportelli, A. Del Guerra, V. Rosso, Journal of Instrumentation 10 (C01010) (2015) 1. http://dx.doi.org/10.1088/1748-0221/10/01/C0101.